Environmental Science & Technology

Article

Cite This: Environ. Sci. Technol. 2019, 53, 11588−11596

pubs.acs.org/est

Supercritical CO_2 and CH_4 Uptake by Illite-Smectite Clay Minerals

Junyoung Hwang and Ronny Pini*

Department of Chemical Engineering, Imperial College London, SW7 2AZ London, U.K.

Supporting Information

ABSTRACT: Clay minerals abound in sedimentary formations and the interaction of reservoir gases with their submicron features have direct relevance to many geoenergy applications. The quantification of gas uptake over a broad range of pressures is key toward assessing the significance of these physical interactions on enhancing storage capacity and gas recovery. We report a systematic investigation of the sorption properties of three source clay minerals—Na-rich montmorillonite (SWy-2), illite-smectite mixed layer (ISCz-1), and illite (IMt-2)—using CO_2 and CH_4 up to 30 MPa at 25−115 °C. The textural characterization of the clays by gas physisorption indicates that micropores are only partly accessible to N_2 (77 K) and Ar (87 K), while larger uptakes are measured with CO_2 (273 K) in the presence of illite. The supercritical excess sorption experiments confirm these findings while revealing differences in uptake capacities that originate from the clay-specific pore size distribution. The lattice density functional theory model describes accurately the measured sorption isotherms by using a distribution of properly weighted slit pores and clay-specific solid−fluid interaction energies, which agree with isosteric heats of adsorption obtained experimentally. The model indicates that the maximum degree of pore occupancy is universal to the three clays and the two gases, and it depends solely on temperature, reaching values near unity at the critical temperature. These observations greatly support the model's predictive capability for estimating gas adsorption on clay-bearing rocks and sediments.

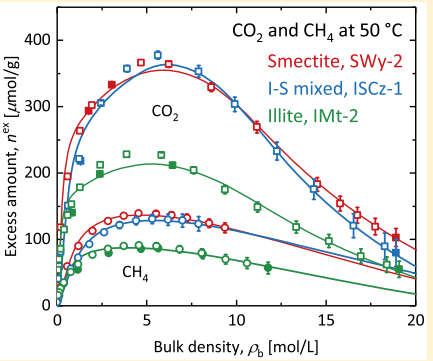

INTRODUCTION

The physical interactions between clay minerals and supercritical gases, particularly CO_2 and CH_4, have received increasing attention in the context of geological carbon storage and unconventional hydrocarbon recovery.[1,2] Clay minerals are very common in geological formations (~30 wt % of all sedimentary rocks[3]) and are present in large fractions in shales (~30 to 90 wt %)[4−7] and oil sands (up to ~80 wt %).[8−12] The presence of clays contributes largely to submicron properties of these rocks, including the presence of nanoscale pores with width less than 100 nm. One significant physical interaction within clay nanopores is gas adsorption, which creates a dense adsorbed phase that increases gas storage capacity[5,13] and affects the gas transport through the pore space.[14] In a typical sandstone reservoir (20% porosity with 10−18 wt % clay content), sorption of CO_2 by clay minerals can increase CO_2 storage capacity by up to 20−30% relative to the capacity associated with residual trapping.[15,16] Sorption of CO_2 on the mudstones that form the majority of caprocks has shown to enhance the sealing efficiency and retention potential from retarded diffusion of the gas.[17−19] The excess uptake by adsorption in hydrocarbon shale reservoirs contributes to 20−80% of the total gas-in-place.[20−23] This level of uptake indicates the potential not only for increased CO_2 capacity but also for enhanced release of hydrocarbon gases induced by the preferential adsorption of CO_2.[24,25]

The abundance of clay minerals in shale and mudstones determines their petrophysical properties, such as porosity, permeability, or wettability, to a great extent,[1,26] often allowing their approximation as quartz-clay systems.[27] The adsorption properties of these rocks are also attributed to their clay mineralogy,[13,17,20,28−30] which tends to be dominated by smectite, illite, and illite−smectite mixed layers (I−S clay minerals).[31] Notably, new experimental evidence indicates that CO_2 can access both the internal (i.e., the interlayer space between basal surfaces) and external surface area of clay minerals irrespective of whether a swelling (e.g., smectite)[26,32−35] or a nonswelling (e.g., illite) clay[16] is considered. These observations have prompted research on quantifying the adsorption properties of clay minerals at subsurface conditions, where most gases are in their supercritical state. These experimental data are the key toward evaluating the sealing stability and capacity of potential storage sites upon introduction of supercritical CO_2[36] or to devise injection policies that increase hydrocarbon production from unconventional reservoirs.[25]

The available data sets for supercritical adsorption on I−S clay minerals and rocks dominated by them remain quite scattered, with only a limited number of studies reporting measurements at multiple temperatures and with different gases. The lack of systematic investigations has resulted in conflicting observations in terms of uptake capacity of source clays[37] and its relation with the textural properties, such as

Received: June 19, 2019
Revised: August 29, 2019
Accepted: September 3, 2019
Published: September 3, 2019

DOI: 10.1021/acs.est.9b03638
Environ. Sci. Technol. 2019, 53, 11588−11596

micropore volume and surface area.[28,38,39] Moreover, there is a lack of validation of experimental data at reservoir pressure and temperature against suitable adsorption models that account for the complex pore structure of clay minerals, and the specific fluid−fluid and solid−fluid interactions.[40−42] In this context, the use of a simplistic modeling approach based on the Langmuir equation is problematic as the basic assumptions of the model,[43] such as monolayer adsorption or no adsorbate−adsorbate interactions, are not fulfilled in clay nanopores.

The objective of this study is to quantify the adsorption of supercritical gases on dry I−S clay minerals over a broad range of pressures and across various temperatures, thereby establishing a baseline for future studies on clays and clay-rich rocks with more complex features. To this aim, we measured a comprehensive set of unary adsorption and desorption isotherms of CO_2 and CH_4 on three source clay minerals, SWy-2 (Na-rich montmorillonite from Wyoming, USA), ISCz-1 (illite-smectite mixed layers from Slovakia), and IMt-2 (illite from Montana, USA) up to 30 MPa at 25, 50, 80, and 115 °C. The structural characterization of the clays was performed via physisorption analysis using N_2, Ar, and CO_2, following the most recent IUPAC guidelines. The supercritical adsorption data were described using the lattice density functional theory (LDFT) model, which uses the pore volumes and pore size distributions (PSD) obtained from the independent textural analysis of the clays as input parameters. The model provides insights into the uptake of supercritical CO_2 and CH_4 within clay nanopores, including pore size-dependent adsorption behaviors and filling capacities. These features are the key toward describing supercritical adsorption on clay minerals and clay-bearing rocks that are characterized by a wide range of micro- and mesoporosity.

MATERIALS AND EXPERIMENTAL METHODS

The clay samples, SWy-2, ISCz-1, and IMt-2, have been sourced from the Source Clay Repository of the Clay Minerals Society (Virginia, USA) and were ground to particles smaller than 50 μm. The samples were degassed ex situ at 200 °C for at least 12 h prior to the measurements. At this degassing temperature, strongly bound water molecules are moved from within the nanostructure of clay minerals[6,44] resulting in reproducible measurements of surface areas.[45] The pure gases were obtained from BOC (Surrey, UK) at purities of 99.9992% for N_2, 99.999% for Ar and He, 99.995% for CO_2, and 99.5% for CH_4. The critical properties of the adsorbates are reported in the Supporting Information.

Gas Adsorption Experiments. The textural properties of the clay minerals were characterized by low-pressure adsorption and desorption experiments using N_2 (77 K) and Ar (87 K) for micro- and mesopore analyses and CO_2 (273 K) for further micropore analysis as recommended by the most recent IUPAC guidelines.[46] The experiments were performed in the pressure range of 3×10^{-7} to 1×10^{-1} MPa using Autosorb iQ (Quantachrome Instruments, Florida, USA) equipped with the CryoSync module, which enables achieving cryogenic temperatures above the standard boiling point temperature of N_2 (77 K). For experiments with CO_2, a liquid circulating thermostat (Julabo CORIO CD-200F, Seelbach, Germany) was used to control the temperature of a bath containing a water−ethylene glycol (50 vol %) mixture. The high-pressure adsorption measurements of CO_2 and CH_4 have been performed in the pressure range of 0.02−30 MPa at 25, 50, 80, and 115 °C using a gravimetric sorption analyzer with a magnetic suspension balance (IsoSORP HPII) from Rubotherm (Bochum, Germany). The measured quantity in these experiments is the excess amount adsorbed,[47] which represents the amount of the adsorbate found in the pore space in addition to the amount that would be present as a bulk supercritical fluid in the same pore space at the given pressure and temperature. The details of the setup, experimental protocols, and the working principles of the magnetic suspension balance have been described in our recent work[37] and are again summarized in the Supporting Information.

MODELING

LDFT Model for Supercritical Adsorption. The LDFT model for single-component adsorption was used in this study to describe the excess adsorption of supercritical CO_2 and CH_4. Briefly, this model discretizes the internal space of adsorbents using a distribution of properly weighted model pores of simple geometries (slit pores in this study) so that fluid molecules form a regular lattice pattern (see Figure S6). The lattice theory was first introduced by Ono and Kondo[48] and later formalized by Aranovich and Donohue,[49] enabling its application to supercritical adsorption systems.[50−52] The LDFT model has been adapted to estimate the adsorbent−adsorbate interaction energies[53−56] and to examine the adsorbed layer densities.[52] The capability of the model highlighted in this study is the incorporation of PSDs, making it suitable for understanding adsorption on clay minerals characterized by both micro- and mesoporosity. The LDFT model has also compared well with the grand canonical Monte Carlo (GCMC) simulations,[50,57,58] showing its reliability and efficiency with less computation time.

The lattice occupancy of the jth layer inside a slit pore with J lattice layers can be calculated from solving the following set of nonlinear equations[51]

$$0 = \epsilon_{sf} + \epsilon_{ff}(z_2\theta_{j+1} + z_1\theta_j - z_0\theta_b) + kT \ln\left(\frac{\theta_j(1-\theta_b)}{\theta_b(1-\theta_j)}\right) \quad \text{for } j = 1 \tag{1}$$

$$0 = \epsilon_{ff}(z_2\theta_{j-1} + z_2\theta_{j+1} + z_1\theta_j - z_0\theta_b) + kT \ln\left(\frac{\theta_j(1-\theta_b)}{\theta_b(1-\theta_j)}\right) \quad \text{for } 1 < j < J \tag{2}$$

$$0 = \epsilon_{sf} + \epsilon_{ff}(z_2\theta_{j-1} + z_1\theta_j - z_0\theta_b) + kT \ln\left(\frac{\theta_j(1-\theta_b)}{\theta_b(1-\theta_j)}\right) \quad \text{for } j = J \tag{3}$$

where ϵ_{sf} and ϵ_{ff} are surface−adsorbate and adsorbate−adsorbate interaction energies, respectively, between nearest neighbors; z_2, z_1, and z_0 (3, 6, and 12) are coordination numbers of the assumed hexagonal lattice configuration; θ_j and θ_b are degrees of lattice occupancy in the jth layer and bulk, respectively; k is Boltzmann's constant; and T is temperature. The excess amount adsorbed is calculated as follows[37]

$$n^{ex}_{LDFT} = c_{sat} \sum_{i=1}^{I} \frac{v_{pore,i}}{J_i} \sum_{j=1}^{J} [\rho_j(\rho_c, \rho_{max}, \theta_j) - \rho_b(\rho_c, \rho_{max}, \theta_b)] \tag{4}$$

DOI: 10.1021/acs.est.9b03638
Environ. Sci. Technol. 2019, 53, 11588−11596

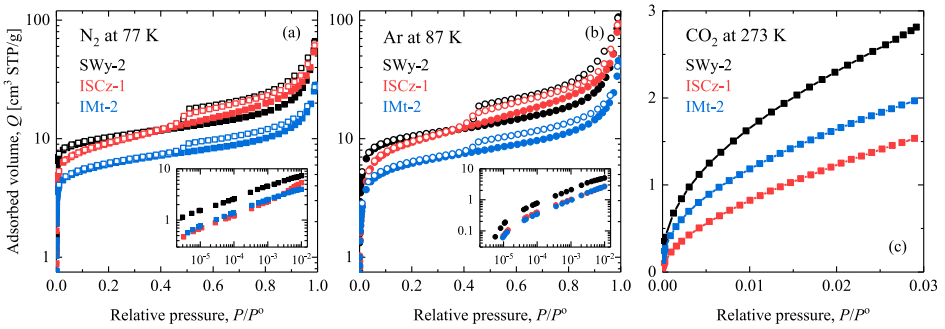

Figure 1. Adsorption (closed symbols) and desorption (open symbols) isotherms of (a) N_2 at 77 K and (b) Ar at 87 K on the clay minerals. The inset plots show the filling of the micropores for $P/P^\circ < 0.01$. (c) Adsorption isotherms of CO_2 at 273 K up to 760Torr ($P/P^\circ \approx 0.03$). The lines are to guide the eye. The values of P° for N_2 (at 77 K), Ar (at 87 K), and CO_2 (at 273 K) are approximately 760, 760, and 26141 mmHg, respectively.

Table 1. Summary of the Textural Properties of SWy-2, ISCz-1, and IMt-2[a]

property	probe gas	unit	SWy-2	ISCz-1	IMt-2
Pore volume[b]	N_2	cm^3/g	0.080	0.078	0.036
	Ar	cm^3/g	0.110	0.101	0.044
micropore	N_2	cm^3/g	0.007	0.001	0.003
	Ar	cm^3/g	0.008	0.003	0.004
	CO_2[c]	cm^3/g	0.009	0.006	0.007
mesopore	N_2	cm^3/g	0.055	0.062	0.026
	Ar	cm^3/g	0.059	0.064	0.026
macropore	N_2	cm^3/g	0.018	0.015	0.007
	Ar	cm^3/g	0.043	0.034	0.014
Specific surface area					
BET	N_2	m^2/g	36.59 ± 0.06	32.38 ± 0.10	21.66 ± 0.09
	Ar	m^2/g	33.38 ± 0.14	30.38 ± 0.16	19.80 ± 0.06
Skeletal density					
He gravimetry	He	g/cm^3	2.709 ± 0.006	2.689 ± 0.009	2.784 ± 0.004

[a]The methods applied to estimate these properties are described in the Supporting Information. [b]NLDFT on the zeolite cylindrical pore model. [c]GCMC on the carbon slit pore model.

where $v_{pore,i}$ is the specific pore volume of lattice pores with J_i layers, and I is the number of lattice pore classes used in the model. The latter is obtained from discretization of experimental PSDs (see Figures S5 and S7). To convert lattice occupancy into density, a mapping function is used that is parameterized in terms of the critical density, ρ_c, and maximum packing density, ρ_{max}.[50] The calculated values of n^{ex} are corrected by a saturation factor, c_{sat}, to account for packing inefficiencies. For each clay mineral, values of c_{sat} (adsorbate- and temperature-dependent), ρ_{max}, and ϵ_{sf} (both adsorbate-dependent) are obtained by fitting eq 4 to the experimental data (see the Supporting Information for details on the numerical solution procedure and the minimization problem).

Isosteric Enthalpy of Adsorption. The isosteric enthalpy of adsorption, Δh, is commonly used to quantify the strength of adsorbate−adsorbent bonding, thereby revealing useful insights on the nature of the adsorbent and adsorbed phase.[43] To this aim, the experimental sorption isotherms are described using the following form of the virial equation[59]

$$\ln(P/n) = \frac{1}{T}\sum_{i=0}^{m_a} a_i n^i + \sum_{i=0}^{m_b} b_i n^i \quad (5)$$

where P is pressure, and a_i and b_i are temperature-independent virial coefficients. Equation 5 can be applied to excess quantities directly but only up to moderate densities.[37,60,61] In this study, we have used the density range, $\rho_b \leq 0.1 \times \rho_{liq}$, corresponding to about 5 MPa for CO_2 and 8 MPa for CH_4. Under these conditions, GCMC simulation results on shale rocks[62] confirm that there is no significant deviation between excess and absolute quantities. Henry's constant is estimated from the zeroth order coefficients, $K_H = \exp[-(a_0/T + b_0)]$, while the isosteric heat of adsorption at zero coverage is obtained from the temperature dependence of K_H

$$|\Delta h_0| = R\left[\frac{\mathrm{d}\ln(K_H)}{\mathrm{d}(1/T)}\right] \quad (6)$$

where R is the ideal gas constant. Accordingly, the isosteric heat of adsorption as a function of loading can be estimated from the adsorption isosteres[59]

$$|\Delta h(n)| = -R\left[\frac{\mathrm{d}\ln(P)}{\mathrm{d}(1/T)}\right]_n = -R\sum_{i=0}^{m} a_i n^i \quad (7)$$

RESULTS AND DISCUSSION

Textural Properties of I−S Clay Minerals. Clays contain nanopores of varied sizes, including micro- (<2 nm), meso- (2−50 nm), and macropores (>50 nm). With reference to Bergaya and Lagaly,[63] these are largely associated with the so-called interlayer regions, as well as voids created through the assembly of clay mineral particles and their aggregates. The physisorption isotherms of N_2 (77 K), Ar (87 K), and CO_2

DOI: 10.1021/acs.est.9b03638
Environ. Sci. Technol. 2019, 53, 11588−11596

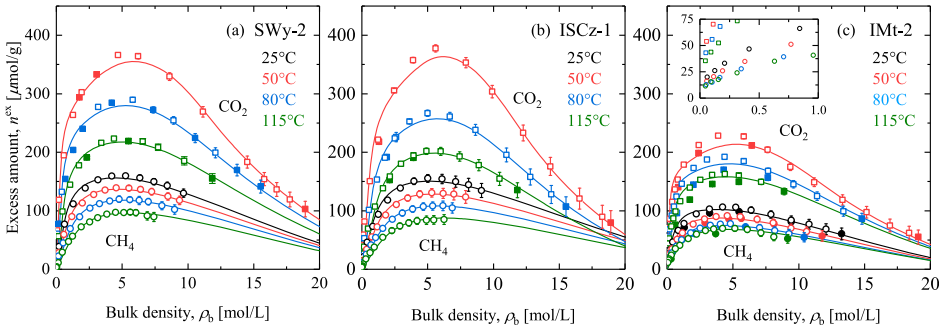

Figure 2. Supercritical adsorption (closed symbols) and desorption (open symbols) of CO_2 (squares) and CH_4 (circles) on (a) SWy-2, (b) ISCz-1, and (c) IMt-2 up to 30 MPa at 25, 50, 80, and 115 °C. The inset plot of (c) shows the desorption points of IMt-2 under 1 mol/L. The solid lines are the LDFT model fits. The following fitted model parameters were obtained for SWy-2, ISCz-1, and IMt-2, respectively: ϵ_{sf}/k = −1131.3, −898.3, and −1277.2 K for CO_2 and -859.5, −771.1, and 969.7 K for CH_4 and ρ_{max} = 26.95, 24.78, and 25.43 mol/L for CO_2 and 26.45, 28.78, and 24.13 mol/L for CH_4.

(273 K) for SWy-2, ISCz-1, and IMt-2 are shown in Figure 1. The shapes of both N_2 and Ar isotherms for all three clay minerals indicate the presence of a cavitation-induced H3 hysteresis loop that closes around $P/P^\circ \approx 0.4$; this type of isotherms implies that these materials consist of a fair amount of small mesopores[6,64] and is characteristic of slit-shaped pores,[46] which in clays are formed by the stacking of platy mineral particles. The steeper increase of the isotherms measured on ISCz-1 for $P/P^\circ > 0.01$ suggests a broader mesopore distribution as compared to SWy-2 and IMt-2. The inset plots of Figure 1a,b reveal appreciable adsorbed amounts in micropores ($P/P^\circ < 0.01$) with SWy-2 showing the largest amount adsorbed compared to the other two clays. This trend is better identified through the measurements with CO_2 (Figure 1c), for which the strength of adsorption increases in the order of ISCz-1 < IMt-2 < SWy-2.

These experimental observations are verified by the pore volumes of the clay minerals computed using the nonlocal density functional theory (NLDFT, for N_2 and Ar) and summarized in Table 1. The corresponding PSDs are reported in the Supporting Information (Figure S5). The total pore volume of the clay minerals increases in the order IMt-2 < ISCz-1 < SWy-2 with values estimated using Ar as the probing gas being systematically larger (20−40% for the total pore volume) than those obtained from N_2 measurements across the entire PSD (micro-, meso-, and macropores). Notably, ISCz-1 shows the largest mesopore volume and a broader distribution of mesoporosity, while SWy-2 and IMt-2 show larger micropore volumes (contributing to 8 and 16% of the total pore volume, respectively). These observations highlight that the textural properties of mixed layer clay particles (ISCz-1) are not the result of the simple combination of the properties of the constituent layers.

The specific surface areas (SSA) obtained by the application of the BET equation[65] are also summarized in Table 1. A good agreement is observed between estimates from N_2 and Ar measurements (6−9% relative difference), which also show a positive correlation with the measured total pore volume. The estimated SSA values are consistent with those reported in the literature[5,6,66−69] but significantly smaller than those obtained by liquid adsorption (~100 m^2/g for illite and ~500 m^2/g for montmorillonite[45]). While it is known that micropores in clays are only partly accessible to N_2, we show here for the first time that the same is true for Ar, thereby confirming that kinetics restrictions in very narrow micropores are present at cryogenic temperatures (77 and 87 K).[46] Interestingly, an excellent agreement is found for IMt-2 between crystallographic skeleton density values[70] (ρ_{cryst} = 2.780 g/cm^3) and values measured by He gravimetry (ρ_{sk} = 2.784 g/cm^3). However, a significant discrepancy is observed for SWy-2 (ρ_{sk} = 2.709 g/cm^3 < ρ_{cryst} = 2.798 g/cm^3[70]), indicating micropore inaccessibility to He. This peculiar pore accessibility in clays is also reflected in the micropore volumes obtained from CO_2 isotherms (using GCMC), which are 10% (SWy-2), 80% (IMt-2), and 100% (ISCz-1) larger than the values obtained using Ar. These observations highlight the importance of conducting physisorption analyses with multiple probing gases to correctly represent the pore volumes of each pore class—micropores by CO_2 and mesopores by N_2 and Ar—in developing adsorption models that use such textural information.

Supercritical Adsorption Isotherms of CO_2 and CH_4. The excess adsorption and desorption isotherms of supercritical CO_2 and CH_4 on SWy-2, ISCz-1, and IMt-2 at four temperatures (25−115 °C) up to 30 MPa are presented in Figure 2 as a function of the bulk fluid density. The full set of experimental data (excess amount adsorbed, measured density, and pressure) are also reported in the Supporting Information (Figure S9 and Table S2−S5). For the three clays and for both gases, the excess isotherms are positive, indicating that sorption contributes to gas storage inside clay nanopores throughout the entire pressure range investigated. While all the measured isotherms possess the nonmonotonic behavior that is characteristic of excess adsorption data, they also reveal subtle differences that originate from the clay-specific PSD discussed above. SWy-2 and ISCz-1 show similar uptake capacities and their isotherm shapes resemble that of a mesoporous material, such as silica gel,[50,71] where the gradual increase in the adsorbed amount reaches a maximum at $\rho_b \geq 5$ mol/L. However, the larger fraction of mesopores in ISCz-1 is also responsible for the characteristic pore-filling mechanism that produces a stronger dependence of the adsorbed amount on temperature compared to SWy-2 (particularly evident for the CO_2 isotherms measured at 50 and 80 °C). Smaller CO_2 and CH_4 uptakes are observed for IMt-2, reflecting its smaller total pore volume. However, the large fraction of micropores of IMt-2 results in a steep initial increase of the measured isotherms that is indeed typical of microporous materials.[60,72−74] Interestingly, the isotherms of IMt-2 also show moderate, but not negligible, hystereses for both CO_2 and CH_4 at all temperatures. Previous observations of hysteresis at super-

DOI: 10.1021/acs.est.9b03638
Environ. Sci. Technol. 2019, 53, 11588−11596

Table 2. Comparison of the Calculated Adsorbed Densities of CO_2 and CH_4 with Their Respective Liquid Densities

							ρ_{LDFT}[b] [mol/L]		
fluid	P [bar]	T [°C]	ρ_{liq} [mol/L]	P [bar]	T [°C]	ρ_{GCMC}[75a] [mol/L]	SWy-2	ISCz-1	IMt-2
CO_2	5.187	−56.56	26.78	150	60	25.53	22.09	20.52	21.35
CH_4	1.013	−161.48	26.33	150	60	17.42	15.26	15.26	15.09

[a]The area between the first two peaks of a density profile inside slit pores with structureless carbon surfaces simulated by GCMC. [b]The average density of the first two adsorbed layers.

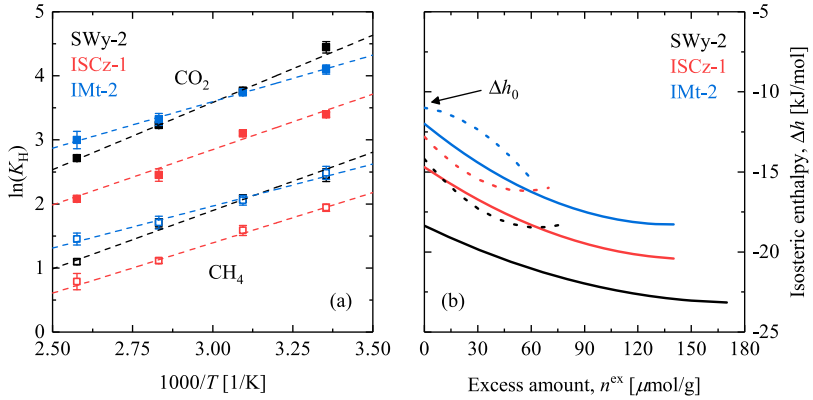

Figure 3. (a) $\ln(K_H)$ plotted against the inverse temperature, $1/T$, for CO_2 (closed symbols) and CH_4 (open symbols). The dashed lines are linear fits to obtain the isosteric enthalpy of adsorption at zero coverage. (b) Isosteric enthalpy of adsorption of CO_2 (solid lines) and CH_4 (dotted lines) plotted against excess amounts of adsorption.

Table 3. Henry's Constants, Selectivity, and Enthalpy of Adsorption at Zero Coverage for CO_2 and CH_4 Adsorption on SWy-2, ISCZ-1, and IMt-2

sample	T [°C]	K_{H,CO_2} [μmol/g·bar]	K_{H,CH_4} [μmol/g·bar]	S [-]	Δh_0 CO_2 [kJ/mol]	Δh_0 CH_4 [kJ/mol]
SWy-2	25	85.3 ± 8.0	11.6 ± 1.2	7.4 ± 1.0	−18.4 ± 0.6	−14.2 ± 0.7
	50	43.3 ± 1.1	8.1 ± 0.5	5.3 ± 0.4		
	80	25.3 ± 0.9	5.5 ± 0.4	4.6 ± 0.4		
	115	15.1 ± 0.7	3.0 ± 0.1	5.0 ± 0.3		
ISCz-1	25	29.8 ± 1.2	7.0 ± 0.4	4.3 ± 0.3	−14.7 ± 0.4	−12.8 ± 0.9
	50	22.2 ± 0.8	4.9 ± 0.4	4.5 ± 0.4		
	80	11.6 ± 1.2	3.0 ± 0.1	3.9 ± 0.4		
	115	8.0 ± 0.4	2.2 ± 0.3	3.6 ± 0.5		
IMt-2	25	60.2 ± 4.5	12.0 ± 1.3	5.0 ± 0.7	−12.0 ± 0.9	−11.0 ± 0.8
	50	42.1 ± 1.4	7.8 ± 0.6	5.4 ± 0.5		
	80	27.6 ± 2.7	5.5 ± 0.6	5.0 ± 0.7		
	115	20.0 ± 2.9	4.3 ± 0.4	4.7 ± 0.8		

critical conditions have been limited to swelling clay minerals, such as smectite,[39,75] the microstructure of which is sensitive to the water content.[76] Because IMt-2 is nonswelling, we attribute this observation to strongly attached CO_2 and CH_4 that are only removed at sufficiently high temperatures. The supercritical desorption isotherms indeed show sorbed amounts of both gases that persist between 10 and 50 μmol/g at approximately 1.5 bar (inset of Figure 2c). Recent findings have revealed CO_2 interlayer trapping in muscovite (used as a proxy for illite) following incubation at 12 MPa and 90 °C.[16] While they are not sufficient to define the controlling mechanisms for this phenomenon, our sorption results support these observations and extend them to CH_4, while covering a broader range of temperature and pressure.

Adsorption Model. The LDFT model incorporates the materials' PSDs and correctly describes the experimental isotherms as can be seen from the solid lines in Figure 2. Both adsorption and desorption data were used in fitting the isotherms of SWy-2 and ISCz-1, but only desorption data were used for IMt-2 because of the hysteresis loops and the limited amount of adsorption data. The values of the fitted parameters, ϵ_{sf} and ρ_{max}, are given in the caption of Figure 2. The attainment of ρ_{max} corresponds to the complete filling of the lattice, at which the adsorbed density is equal to the bulk density. Comparable values were found for all three clay minerals for both CO_2 and CH_4, namely, ρ_{max} = 25.72 ± 1.23 mol/L for CO_2 and ρ_{max} = 25.72 ± 1.23 mol/L, corresponding to $\rho_{max}/\rho_c \approx 2.5$. These values agree well with those previously reported from the application of the LDFT model for CO_2 and CH_4 on activated carbon,[52,53] as well as with the liquid densities at triple point CO_2 and standard boiling point of CH_4 (Table 2). However, as indicated by GCMC simulations of supercritical adsorption in shale,[75] adsorbed phase densities are not constant and may differ from the saturated liquid densities. The LDFT model shows a similar behavior as summarized in Table 2, where the average density values of the first two adsorbed layers in each clay mineral are reported for both CO_2 and CH_4. While for CO_2, the obtained values are about 20%

DOI: 10.1021/acs.est.9b03638
Environ. Sci. Technol. 2019, 53, 11588−11596

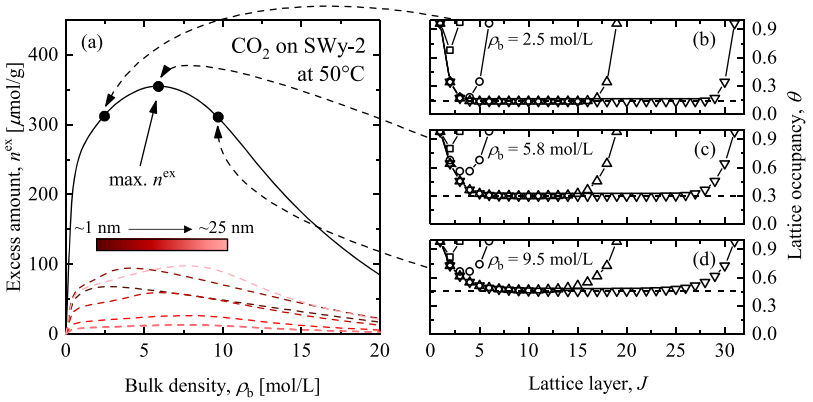

Figure 4. (a) CO_2 adsorption isotherm at 50 °C on SWy-2 (solid line) with isotherms of individual pores (dashed lines) in color. The pore sizes of the individual isotherms are indicated by the color scale. (b–d) Lattice occupancy profiles corresponding to three density values highlighted in (a)—maximum amount of adsorption, n^{ex}_{max}, and points before and after n^{ex}_{max} with the same amount of excess adsorption—for the lattice pores with 3 (1.2 nm, square), 6 (2.4 nm, circle), 19 (7.6 nm, upward triangle), and 31 (12.4 nm, downward triangle) layers.

below the saturated liquid density, the estimates for CH_4 are even lower (40%), reflecting the equilibration with a bulk phase that has a lower density under the same temperature and pressure conditions. For CH_4 on illite, adsorbed densities obtained by GCMC simulations (13.1–14.3 mol/L) reveal that this phenomenon persists even at a higher pressure (30 MPa at 90 °C).[77]

Adsorption Energetics. Henry's constants, K_H, were obtained by describing the experimental data with eq 5. The plots of $\ln(K_H)$ against $1/T$ (Figure 3a) show good fits to linear regression (R^2 = 0.967–0.996), and the discernible linear regions of the virial plots (Figure S8a–c) validate the suitability of the approach to estimate Henry's constants. The data are summarized in Table 3 together with estimates of Δh_0 calculated from eq 6 and the selectivity of CO_2 to CH_4 ($S = K_{H,CO_2}/K_{H,CH_4}$).

The values of $|\Delta h_0|$ decrease from SWy-2 to IMt-2 consistent with estimates by Ji et al.[78] for CH_4 on rocks each dominated by clays in this study. While $|\Delta h_0|$ is expected to increase with the decreasing pore diameter,[79] IMt-2 shows the lowest value of $|\Delta h_0|$ despite its larger fraction of micropores. This suggests that adsorption energetics in clays may be additionally affected by other factors, such as the surface chemistry, as indicated by the observed decrease of $|\Delta h_0|$ with increasing illite content.[78] These values are also on the lower end of the range indicated by the general approximation proposed for gas physisorption,[80] that is $|\Delta h_0| < 1.5–2|\Delta h_{vap}|$, where $|\Delta h_{vap}|$ is the latent heat of condensation (10.3 kJ/mol for CO_2 at 273.15 K and 8.2 kJ/mol for CH_4 at 112 K[81]). The estimates of Δh_0 obtained from the LDFT model in Henry's region (up to 0.3 bar) do not reveal any specific trend among the three clays ($|\Delta h^{LDFT}_{0,CO_2}| \approx 16.3 \pm 0.8$ kJ/mol and $|\Delta h^{LDFT}_{0,CH_4}| \approx 13.1 \pm 0.5$ kJ/mol). Most significantly, they compare well with their experimental counterparts, and the observed discrepancy for IMt-2 is likely due to the model's description of the large sorption amounts in the low-pressure regions that cause hystereses, as discussed earlier. Notably, the ratio of CO_2 to CH_4 is correctly described by the model, that is $\Delta h_{0,CO_2}/\Delta h_{0,CH_4} \approx \Delta h^{LDFT}_{0,CO_2}/\Delta h^{LDFT}_{0,CH_4} \approx 1.2 \pm 0.1$.

Figure 3b indicates that $|\Delta h|$ increases as a function of loading by approximately 5–6 and 3–4 kJ/mol for CO_2 and CH_4, respectively. This behavior is the result of increasing lateral adsorbate interactions on relatively homogeneous surfaces[73,82,83] of clay minerals as opposed to heterogeneous shales that show decreasing $|\Delta h|$ for CO_2 and CH_4.[84] Notably, we do not observe the expected enhancement in the change of $|\Delta h|$ with loading due to molecular polarity,[43] as CO_2 and CH_4 outline a similar behavior. This may partly be due to the limited range of densities used in the analysis.

The analysis of the adsorption energetics indicate that the three clay minerals are appropriate for enhanced CH_4 recovery through the injection of CO_2 as the released heat from CO_2 adsorption will lead to desorption of CH_4. The thermodynamic properties suggest that SWy-2 is most suited among the three clay minerals in this study for the application of CO_2 storage and enhanced recovery. The adsorption enthalpy indicates the strongest interaction with CO_2 and the highest average selectivity of CO_2 over CH_4. It should be highlighted that these conclusions apply to thoroughly dried clay. While in actual geological formations clays are hydrated, the effect of water on the total extent of adsorption of reservoir gases (and, accordingly, energetics) remains uncertain. Experimental studies have shown that water may either decrease the adsorption capacity by competitively occupying sorption sites or increase it by providing more accessible micropore volume, as a result of clay swelling.[85]

CO_2 and CH_4 in Clay Nanopores. The LDFT model provides insights into the uptake of supercritical CO_2 and CH_4 within clay nanopores including pore size-dependent adsorption behaviors and into the degree of pore occupancy of the supercritical adsorbed phase. Figure 4a shows the CO_2 excess adsorption isotherm on SWy-2 at 50 °C produced by the LDFT model with the individual contributions from each pore class, and Figure 4b–d shows the lattice occupancy profiles for four selected pore classes. It can be seen that the adsorption process is controlled by pore filling (significant density enhancement above that of the bulk phase) up to small mesopores (J = 6, <2.5 nm); for pores larger (upward and downward triangles), multiple layers are formed as the bulk density increases, while the center of the pore remains filled with bulk supercritical fluids. This observation of pore size-specific behavior compares well with the supercritical sorption mechanism shown by GCMC simulations[77,86,87] inside slit pores of clay minerals, in which the filling of adsorbates occurs for micropores, while the adsorption layers on the surface dominate the adsorption behavior for larger mesopores. The

DOI: 10.1021/acs.est.9b03638
Environ. Sci. Technol. 2019, 53, 11588–11596

observed difference in the extent of fluid densification inside pores suggests that supercritical adsorption on clay mineral surfaces should not be assessed using a single pore system.

Figure 5 shows the pore saturation factors, c_{sat}, plotted against the reciprocal of reduced temperature, T_c/T. It can be

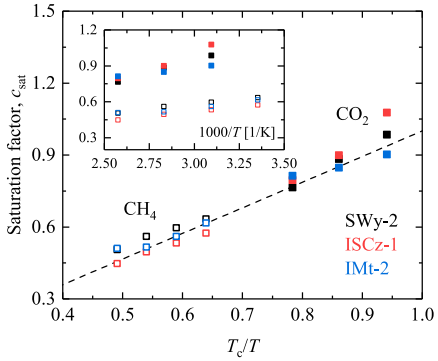

Figure 5. Saturation factors of CO_2 (closed symbols) and CH_4 (open symbols) as a function of T_c/T. The inset plot shows the same values against $1/T$. The linear regression of the data shown in the plot can be described by $c_{sat} = 1.07(T_c/T) - 0.07$. The value of c_{sat} of ISCz-1 at 50 °C was omitted in linear regression for the reason discussed in the main text, and the intercept was corrected to equate the value of c_{sat} to unity as T_c/T approaches unity.

seen that c_{sat} increases linearly with values approaching unity as the critical temperature of the fluid is reached. This reduction as T increases beyond T_c suggests that the adsorbed fluid does not occupy the entire space of the pore volume at these conditions, and c_{sat} accounts for the temperature-dependent variability of the packing density in the LDFT model. Bénard and Chahine[53] and Do[88] similarly explained the phenomenon by attributing it to the compressibility and thermal expansion characteristics of the adsorbed phase that becomes greater above the critical temperature. It should be noted that the value of c_{sat} for CO_2 on ISCz-1 at 50 °C is above 1, although it is considered to be physically implausible by the definition provided in this study. This again highlights the difficulty to accurately measure the PSD of clay minerals and may indicate the enhanced accessibility of gases, such as CO_2, in clay nanopores. The most relevant observation is that the three clay minerals and the two gases outline a single characteristic line (Figure 5), suggesting that the degree of occupancy depends solely on temperature. This observation of temperature dependence drawn from multiple samples greatly extends the predictive capability of the model for supercritical adsorption on clay-bearing geosorbents.

■ ASSOCIATED CONTENT

Supporting Information

The Supporting Information is available free of charge on the ACS Publications website at DOI: 10.1021/acs.est.9b03638.

Sample preparation, adsorbate properties, high-pressure sorption experiments, low-pressure physisorption experiments, LDFT model, viriral plots, and high-pressure sorption data (PDF)

■ AUTHOR INFORMATION

Corresponding Author

*E-mail: r.pini@imperial.ac.uk.

ORCID

Junyoung Hwang: 0000-0003-1867-8461

Ronny Pini: 0000-0002-9443-3573

Notes

The authors declare no competing financial interest.

■ ACKNOWLEDGMENTS

This work is part of the Science4CleanEnergy European research consortium funded by European Union's Horizon 2020 research and innovation programme under grant agreement no. 764810 (S4CE). J.H. was funded by a departmental scholarship from the Department of Chemical Engineering, Imperial College London.

■ REFERENCES

(1) Bourg, I. C.; Beckingham, L. E.; DePaolo, D. J. The Nanoscale Basis of CO_2 Trapping for Geologic Storage. *Environ. Sci. Technol.* **2015**, *49*, 10265−10284.

(2) Rutter, E.; Mecklenburgh, J.; Taylor, K. Geomechanical and petrophysical properties of mudrocks: introduction. *Geol. Soc. London Spec. Publ.* **2017**, *454*, 1−13.

(3) Lynch, F. L. Frio Shale mineralogy and the stoichiometry of the smectite-to-illite reaction: the most important reaction in clastic sedimentary diagenesis. *Clays Clay Miner.* **1997**, *45*, 618−631.

(4) Kwon, O.; Kronenberg, A. K.; Gangi, A. F.; Johnson, B. Permeability of Wilcox shale and its effective pressure law. *J. Geophys. Res.* **2001**, *106*, 19339−19353.

(5) Busch, A.; Alles, S.; Gensterblum, Y.; Prinz, D.; Dewhurst, D.; Raven, M.; Stanjek, H.; Krooss, B. Carbon dioxide storage potential of shales. *Int. J. Greenhouse Gas Control* **2008**, *2*, 297−308.

(6) Kuila, U.; Prasad, M. Specific surface area and pore-size distribution in clays and shales. *Geophys. Prospect.* **2013**, *61*, 341−362.

(7) Sone, H.; Zoback, M. D. Mechanical properties of shale-gas reservoir rocks—part 1: static and dynamic elastic properties and anisotropy. *Geophysics* **2013**, *78*, D381−D392.

(8) Omotoso, O.; Mikula, R. J. High surface areas caused by smectitic interstratification of kaolinite and illite in Athabasca oil sands. *Appl. Clay Sci.* **2004**, *25*, 37−47.

(9) Mercier, P. H. J.; Patarachao, B.; Kung, J.; Kingston, D. M.; Woods, J. R.; Sparks, B. D.; Kotlyar, L. S.; Ng, S.; Moran, K.; McCracken, T. X-ray diffraction (XRD)-derived processability markers for oil sands based on clay mineralogy and crystallite thickness distributions. *Energy Fuels* **2008**, *22*, 3174−3193.

(10) Osacky, M.; Geramian, M.; Ivey, D. G.; Liu, Q.; Etsell, T. H. Mineralogical and chemical composition of petrologic end members of Alberta oil sands. *Fuel* **2013**, *113*, 148−157.

(11) Geramian, M.; Osacky, M.; Ivey, D. G.; Liu, Q.; Etsell, T. H. Effect of swelling clay minerals (montmorillonite and illite-smectite) on nonaqueous bitumen extraction from Alberta oil sands. *Energy Fuels* **2016**, *30*, 8083−8090.

(12) Entezari, I.; Rivard, B.; Geramian, M.; Lipsett, M. G. Predicting the abundance of clays and quartz in oil sands using hyperspectral measurements. *Int. J. Appl. Earth Obs. Geoinf.* **2017**, *59*, 1−8.

(13) Heller, R.; Zoback, M. Adsorption of methane and carbon dioxide on gas shale and pure mineral samples. *Journal of Unconventional Oil and Gas Resources* **2014**, *8*, 14−24.

(14) Song, J.; Zhang, D. Comprehensive review of caprock-sealing mechanisms for geologic carbon sequestration. *Environ. Sci. Technol.* **2013**, *47*, 9−22.

(15) Busch, A.; Bertier, P.; Gensterblum, Y.; Rother, G.; Spiers, C. J.; Zhang, M.; Wentinck, H. M. On sorption and swelling of CO_2 in clays. *Geomechanics and Geophysics for Geo-energy and Geo-resources* **2016**, *2*, 111−130.

(16) Wan, J.; Tokunaga, T. K.; Ashby, P. D.; Kim, Y.; Voltolini, M.; Gilbert, B.; DePaolo, D. J. Supercritical CO_2 uptake by nonswelling phyllosilicates. *Proc. Natl. Acad. Sci. U.S.A.* **2018**, *115*, 873−878.

DOI: 10.1021/acs.est.9b03638
Environ. Sci. Technol. 2019, 53, 11588−11596

(17) Wollenweber, J.; Alles, S.; Busch, A.; Krooss, B. M.; Stanjek, H.; Littke, R. Experimental investigation of the CO_2 sealing efficiency of caprocks. *Int. J. Greenhouse Gas Control* **2010**, *4*, 231−241.
(18) Amann, A.; Waschbüsch, M.; Bertier, P.; Busch, A.; Krooss, B. M.; Littke, R. Sealing rock characteristics under the influence of CO_2. *Energy Procedia* **2011**, *4*, 5170−5177.
(19) Amann-Hildenbrand, A.; Bertier, P.; Busch, A.; Krooss, B. M. Experimental investigation of the sealing capacity of generic clay-rich caprocks. *Int. J. Greenhouse Gas Control* **2013**, *19*, 620−641.
(20) Lu, X.; Li, F.-C.; Watson, A. T. Adsorption measurements in Devonian shales. *Fuel* **1995**, *74*, 599−603.
(21) Curtis, J. B. Fractured shale-gas systems. *AAPG Bull.* **2002**, *86*, 1921−1938.
(22) Montgomery, S. L.; Jarvie, D. M.; Bowker, K. A.; Pollastro, R. M. Mississippian Barnett Shale, Fort Worth basin, north-central Texas: Gas-shale play with multi-trillion cubic foot potential. *AAPG Bull.* **2005**, *89*, 155−175.
(23) Ambrose, R. J.; Hartman, R. C.; Diaz-Campos, M.; Akkutlu, I. Y.; Sondergeld, C. H. Shale gas-in-place calculations part I: new pore-scale considerations. *SPE J.* **2012**, *17*, 219−229.
(24) Liu, F.; Ellett, K.; Xiao, Y.; Rupp, J. A. Assessing the feasibility of CO_2 storage in the New Albany Shale (Devonian-Mississippian) with potential enhanced gas recovery using reservoir simulation. *Int. J. Greenhouse Gas Control* **2013**, *17*, 111−126.
(25) Middleton, R. S.; Carey, J. W.; Currier, R. P.; Hyman, J. D.; Kang, Q.; Karra, S.; Jiménez-Martínez, J.; Porter, M. L.; Viswanathan, H. S. Shale gas and non-aqueous fracturing fluids: Opportunities and challenges for supercritical CO_2. *Appl. Energy* **2015**, *147*, 500−509.
(26) Ilton, E. S.; Schaef, H. T.; Qafoku, O.; Rosso, K. M.; Felmy, A. R. In Situ X-ray Diffraction Study of Na^+ Saturated Montmorillonite Exposed to Variably Wet Super Critical CO_2. *Environ. Sci. Technol.* **2012**, *46*, 4241−4248.
(27) Cole, D. R.; Chialvo, A. A.; Rother, G.; Vlcek, L.; Cummings, P. T. Supercritical fluid behavior at nanoscale interfaces: Implications for CO_2 sequestration in geologic formations. *Philos. Mag.* **2010**, *90*, 2339−2363.
(28) Ross, D. J. K.; Bustin, R. M. The importance of shale composition and pore structure upon gas storage potential of shale gas reservoirs. *Mar. Pet. Geol.* **2009**, *26*, 916−927.
(29) Zhong, J.; Chen, G.; Lv, C.; Yang, W.; Xu, Y.; Yang, S.; Xue, L. Experimental study of the impact on methane adsorption capacity of continental shales with thermal evolution. *Journal of Natural Gas Geoscience* **2016**, *1*, 165−172.
(30) Zhang, C.; Pathegama Gamage, R.; Perera, M.; Zhao, J. Characteristics of Clay-Abundant Shale Formations: Use of CO_2 for Production Enhancement. *Energies* **2017**, *10*, 1887.
(31) Weaver, C. E. A discussion on the origin of clay minerals in sedimentary rocks. *Clays Clay Miner.* **1956**, *5*, 159−173.
(32) Loring, J. S.; Schaef, H. T.; Turcu, R. V. F.; Thompson, C. J.; Miller, Q. R. S.; Martin, P. F.; Hu, J.; Hoyt, D. W.; Qafoku, O.; Ilton, E. S.; Felmy, A. R.; Rosso, K. M. In Situ Molecular Spectroscopic Evidence for CO_2 Intercalation into Montmorillonite in Supercritical Carbon Dioxide. *Langmuir* **2012**, *28*, 7125−7128.
(33) Schaef, H. T.; Ilton, E. S.; Qafoku, O.; Martin, P. F.; Felmy, A. R.; Rosso, K. M. In situ XRD study of Ca^{2+} saturated montmorillonite (STX-1) exposed to anhydrous and wet supercritical carbon dioxide. *Int. J. Greenhouse Gas Control* **2012**, *6*, 220−229.
(34) Rother, G.; Ilton, E. S.; Wallacher, D.; Hauβ, T.; Schaef, H. T.; Qafoku, O.; Rosso, K. M.; Felmy, A. R.; Krukowski, E. G.; Stack, A. G.; Grimm, N.; Bodnar, R. J. CO_2 Sorption to Subsingle Hydration Layer Montmorillonite Clay Studied by Excess Sorption and Neutron Diffraction Measurements. *Environ. Sci. Technol.* **2013**, *47*, 205−211.
(35) Loganathan, N.; Yazaydin, A. O.; Bowers, G. M.; Kalinichev, A. G.; Kirkpatrick, R. J. Molecular Dynamics Study of CO_2 and H_2O Intercalation in Smectite Clays: Effect of Temperature and Pressure on Interlayer Structure and Dynamics in Hectorite. *J. Phys. Chem. C* **2017**, *121*, 24527−24540.
(36) Busch, A.; Amann-Hildenbrand, A.; Bertier, P.; Waschbuesch, M.; Krooss, B. M. The significance of caprock sealing integrity for CO_2 storage. *SPE International Conference on CO_2 Capture, Storage, and Utilization*, 2010; pp 1−8.
(37) Hwang, J.; Joss, L.; Pini, R. Measuring and modelling supercritical adsorption of CO_2 and CH_4 on montmorillonite source clay. *Microporous Mesoporous Mater.* **2019**, *273*, 107−121.
(38) Liu, D.; Yuan, P.; Liu, H.; Li, T.; Tan, D.; Yuan, W.; He, H. High-pressure adsorption of methane on montmorillonite, kaolinite and illite. *Appl. Clay Sci.* **2013**, *85*, 25−30.
(39) Jeon, P. R.; Choi, J.; Yun, T. S.; Lee, C.-H. Sorption equilibrium and kinetics of CO_2 on clay minerals from subcritical to supercritical conditions: CO_2 sequestration at nanoscale interfaces. *Chem. Eng. J.* **2014**, *255*, 705−715.
(40) Zhang, J.; Clennell, M. B.; Liu, K.; Pervukhina, M.; Chen, G.; Dewhurst, D. N. Methane and carbon dioxide adsorption on Illite. *Energy Fuels* **2016**, *30*, 10643−10652.
(41) Tian, Y.; Yan, C.; Jin, Z. Characterization of methane excess and absolute adsorption in various clay nanopores from molecular simulation. *Sci. Rep.* **2017**, *7*, 12040.
(42) Loganathan, N.; Bowers, G. M.; Ngouana Wakou, B. F.; Kalinichev, A. G.; Kirkpatrick, R. J.; Yazaydin, A. O. Understanding methane/carbon dioxide partitioning in clay nano- and meso-pores with constant reservoir composition molecular dynamics modeling. *Phys. Chem. Chem. Phys.* **2019**, *21*, 6917−6924.
(43) Ruthven, D. M. *Principles of Adsorption and Adsorption Processes*; John Wiley and Sons: New York, 1984.
(44) Środoń, J.; McCarty, D. K. Surface area and layer charge of smectite from CEC and EGME/H_2O-retention measurements. *Clays Clay Miner.* **2008**, *56*, 155−174.
(45) Macht, F.; Eusterhues, K.; Pronk, G. J.; Totsche, K. U. Specific surface area of clay minerals: Comparison between atomic force microscopy measurements and bulk-gas (N_2) and -liquid (EGME) adsorption methods. *Appl. Clay Sci.* **2011**, *53*, 20−26.
(46) Thommes, M.; Kaneko, K.; Neimark, A. V.; Olivier, J. P.; Rodriguez-Reinoso, F.; Rouquerol, J.; Sing, K. S. W. Physisorption of gases, with special reference to the evaluation of surface area and pore size distribution (IUPAC Technical Report). *Pure Appl. Chem.* **2015**, *87*, 1051−1069.
(47) Sircar, S. Measurement of gibbsian surface excess. *AIChE J.* **2001**, *47*, 1169−1176.
(48) Ono, S.; Kondo, S. *Structure of Liquids*; Springer: Berlin, 1960; pp 134−280.
(49) Aranovich, G. L.; Donohue, M. D. Adsorption of supercritical fluids. *J. Colloid Interface Sci.* **1996**, *180*, 537−541.
(50) Hocker, T.; Rajendran, A.; Mazzotti, M. Measuring and Modeling Supercritical Adsorption in Porous Solids. Carbon Dioxide on 13X Zeolite and on Silica Gel. *Langmuir* **2003**, *19*, 1254−1267.
(51) Ottiger, S.; Pini, R.; Storti, G.; Mazzotti, M. Competitive adsorption equilibria of CO_2 and CH_4 on a dry coal. *Adsorption* **2008**, *14*, 539−556.
(52) Sudibandriyo, M.; Mohammad, S. A.; Robinson, R. L.; Gasem, K. A. M. Ono-Kondo lattice model for high-pressure adsorption: Pure gases. *Fluid Phase Equilib.* **2010**, *299*, 238−251.
(53) Bénard, P.; Chahine, R. Modeling of high-pressure adsorption isotherms above the critical temperature on microporous adsorbents: application to methane. *Langmuir* **1997**, *13*, 808−813.
(54) Bénard, P.; Chahine, R. Determination of the Adsorption Isotherms of Hydrogen on Activated Carbons above the Critical Temperature of the Adsorbate over Wide Temperature and Pressure Ranges. *Langmuir* **2001**, *17*, 1950−1955.
(55) Romanos, J.; Abou Dargham, S.; Roukos, R.; Pfeifer, P. Local Pressure of Supercritical Adsorbed Hydrogen in Nanopores. *Materials* **2018**, *11*, 2235.
(56) Romanos, J.; Abou Dargham, S.; Roukos, R.; Pfeifer, P. Properties of adsorbed supercritical methane film in nanopores. *AIP Adv.* **2018**, *8*, 125011.
(57) Pang, W.; Jin, Z. Revisiting methane absolute adsorption in organic nanopores from molecular simulation and Ono-Kondo lattice model. *Fuel* **2019**, *235*, 339−349.

DOI: 10.1021/acs.est.9b03638
Environ. Sci. Technol. 2019, 53, 11588−11596

(58) Pang, W.; Jin, Z. Ono-Kondo lattice model for propane multilayer adsorption in organic nanopores in relation to shale gas. *Fuel* **2019**, *235*, 158−166.
(59) Czepirski, L.; JagieŁŁo, J. Virial-type thermal equation of gas-solid adsorption. *Chem. Eng. Sci.* **1989**, *44*, 797−801.
(60) Schell, J.; Casas, N.; Pini, R.; Mazzotti, M. Pure and binary adsorption of CO_2, H_2, and N_2 on activated carbon. *Adsorption* **2012**, *18*, 49−65.
(61) Stadie, N. Synthesis and thermodynamic studies of physisorption energy storage materials. Ph.D. Thesis, California Institute of Technology, 2013.
(62) Wu, T.; Zhao, H.; Tesson, S.; Firoozabadi, A. Absolute adsorption of light hydrocarbons and carbon dioxide in shale rock and isolated kerogen. *Fuel* **2019**, *235*, 855−867.
(63) Bergaya, F.; Lagaly, G. In *Handbook of Clay Science*, 1st ed.; Bergaya, F., Theng, B. K. G., Lagaly, G., Eds.; Elsevier: Oxford, 2006; Vol. *1*; Chapter 1, pp 1−18.
(64) Groen, J. C.; Peffer, L. A. A.; Pérez-Ramírez, J. Pore size determination in modified micro- and mesoporous materials. Pitfalls and limitations in gas adsorption data analysis. *Microporous Mesoporous Mater.* **2003**, *60*, 1−17.
(65) Brunauer, S.; Emmett, P. H.; Teller, E. Adsorption of Gases in Multimolecular Layers. *J. Am. Chem. Soc.* **1938**, *60*, 309−319.
(66) Cheng, A.-L.; Huang, W.-L. Selective adsorption of hydrocarbon gases on clays and organic matter. *Org. Chem.* **2004**, *35*, 413−423.
(67) Carmody, O.; Frost, R.; Xi, Y.; Kokot, S. Surface characterisation of selected sorbent materials for common hydrocarbon fuels. *Surf. Sci.* **2007**, *601*, 2066−2076.
(68) Dogan, M.; Dogan, A. U.; Yesilyurt, F. I.; Alaygut, D.; Buckner, I.; Wurster, D. E. Baseline studies of The Clay Minerals Society special clays: specific surface area by the Brunauer Emmett Teller (BET) method. *Clays Clay Miner.* **2007**, *55*, 534−541.
(69) Joewondo, N. Pore structure of micro- and mesoporous mudrocks based on nitrogen and carbon dioxide sorption. Master Thesis, Colorado School of Mines, 2018.
(70) Deeds, C. T.; Van Olphen, H. Density studies in clay-liquid systems, part II: application to core analysis. *Clays Clay Miner.* **1961**, *10*, 318−328.
(71) Pini, R.; Ottiger, S.; Rajendran, A.; Storti, G.; Mazzotti, M. Near-critical adsorption of CO_2 on 13X zeolite and N_2O on silica gel: lack of evidence of critical phenomena. *Adsorption* **2008**, *14*, 133−141.
(72) Pini, R. Interpretation of net and excess adsorption isotherms in microporous adsorbents. *Microporous Mesoporous Mater.* **2014**, *187*, 40−52.
(73) Murialdo, M.; Ahn, C. C.; Fultz, B. A thermodynamic investigation of adsorbate-adsorbate interactions of carbon dioxide on nanostructured carbons. *AIChE J.* **2018**, *64*, 1026−1033.
(74) Moellmer, J.; Moeller, A.; Dreisbach, F.; Glaeser, R.; Staudt, R. High pressure adsorption of hydrogen, nitrogen, carbon dioxide and methane on the metal-organic framework HKUST-1. *Microporous Mesoporous Mater.* **2011**, *138*, 140−148.
(75) Zhao, H.; Wu, T.; Firoozabadi, A. High pressure sorption of various hydrocarbons and carbon dioxide in Kimmeridge Blackstone and isolated kerogen. *Fuel* **2018**, *224*, 412−423.
(76) Giesting, P.; Guggenheim, S.; Koster van Groos, A. F.; Busch, A. Interaction of carbon dioxide with Na-exchanged montmorillonite at pressures to 640 bars: Implications for CO_2 sequestration. *Int. J. Greenhouse Gas Control* **2012**, *8*, 73−81.
(77) Chen, G.; Lu, S.; Liu, K.; Han, T.; Xu, C.; Xue, Q.; Shen, B.; Guo, Z. GCMC simulations on the adsorption mechanisms of CH_4 and CO_2 in K-illite and their implications for shale gas exploration and development. *Fuel* **2018**, *224*, 521−528.
(78) Ji, L.; Zhang, T.; Milliken, K. L.; Qu, J.; Zhang, X. Experimental investigation of main controls to methane adsorption in clay-rich rocks. *Appl. Geochem.* **2012**, *27*, 2533−2545.
(79) Myers, A. L. Characterization of nanopores by standard enthalpy and entropy of adsorption of probe molecules. *Colloids Surf., A* **2004**, *241*, 9−14.
(80) Ruthven, D. M. The Rectangular Isotherm Model for Adsorption Kinetics. *Adsorption* **2000**, *6*, 287−291.
(81) Lemmon, E. W.; McLinden, M. O.; Friend, D. G. *Thermophysical Properties of Fluid Systems*; National Institute of Standards and Technology, 1998. https://webbook.nist.gov/chemistry/.
(82) Al-Muhtaseb, S. A.; Ritter, J. A. Roles of Surface Heterogeneity and Lateral Interactions on the Isosteric Heat of Adsorption and Adsorbed Phase Heat Capacity. *J. Phys. Chem. B* **1999**, *103*, 2467−2479.
(83) Yuan, B.; Wu, X.; Chen, Y.; Huang, J.; Luo, H.; Deng, S. Adsorption of CO_2, CH_4, and N_2 on ordered mesoporous carbon: approach for greenhouse gases capture and biogas upgrading. *Environ. Sci. Technol.* **2013**, *47*, 5474−5480.
(84) Duan, S.; Gu, M.; Du, X.; Xian, X. Adsorption equilibrium of CO_2 and CH_4 and their mixture on Sichuan Basin shale. *Energy Fuels* **2016**, *30*, 2248−2256.
(85) Schaef, H. T.; Loring, J. S.; Glezakou, V.-A.; Miller, Q. R. S.; Chen, J.; Owen, A. T.; Lee, M.-S.; Ilton, E. S.; Felmy, A. R.; McGrail, B. P.; Thompson, C. J. Competitive sorption of CO_2 and H_2O in 2:1 layer phyllosilicates. *Geochim. Cosmochim. Acta* **2015**, *161*, 248−257.
(86) Jin, Z.; Firoozabadi, A. Methane and carbon dioxide adsorption in clay-like slit pores by Monte Carlo simulations. *Fluid Phase Equilib.* **2013**, *360*, 456−465.
(87) Chen, G.; Lu, S.; Zhang, J.; Xue, Q.; Han, T.; Xue, H.; Tian, S.; Li, J.; Xu, C.; Pervukhina, M.; Clennell, B. Research of CO_2 and N_2 Adsorption Behavior in K-Illite Slit Pores by GCMC Method. *Sci. Rep.* **2016**, *6*, 1−10.
(88) Do, D. D. In *Series on Chemical Engineering*; Yang, R. T., Ed.; Imperial College Press: London, 1998; Vol. *2*; p 892.

DOI: 10.1021/acs.est.9b03638
Environ. Sci. Technol. 2019, 53, 11588−11596